

Weyl magnons in noncoplanar stacked kagomé antiferromagnets

S. A. Owerre¹

¹*Perimeter Institute for Theoretical Physics, 31 Caroline St. N., Waterloo, Ontario N2L 2Y5, Canada.*

(Dated: September 1, 2022)

We predict the existence of Weyl magnons (WMs) in three-dimensional (3D) noncoplanar stacked kagomé antiferromagnets as realized in real materials. We observe pairs of WM nodes with opposite chirality, which form Weyl cones in 3D momentum space. They result from explicit macroscopically broken time-reversal symmetry (TRS) by the scalar spin chirality of noncoplanar chiral spin textures, which is the only requirement for the existence of WM nodes in this system. We find that the WM nodes are present for antiferromagnetic interlayer coupling. They also possess magnon surface states and potentially a topological thermal Hall effect. In this respect, they are different from those of breathing pyrochlore antiferromagnets that require broken TRS by the magnetic order with no scalar spin chirality. Therefore, the current WMs in 3D noncoplanar chiral antiferromagnets are, indeed, promising candidates towards the first experimental realization of WMs in frustrated magnets.

Introduction–. Geometrically frustrated kagomé antiferromagnets are the most studied quantum magnetic systems in condensed matter physics, due to their unconventional properties such as the possibility of quantum spin liquids [1–3], where magnetic long-range order (LRO) is forbidden by frustrated interactions down to the lowest temperatures. However, emerging experimental studies have shown that various frustrated kagomé antiferromagnets show evidence of intrinsic or magnetic-field-induced LRO at low temperatures [4–8]. The presence of LRO in frustrated kagomé antiferromagnets can be as a result of intrinsic perturbative anisotropy such as the Dzyaloshinskii-Moriya interaction (DMI) [9, 10]. The DMI is a consequence of spin-orbit coupling (SOC) and it is present in magnetic systems that lack an inversion center. Interestingly, it is intrinsic to kagomé materials [4–8, 11–13].

Recently, the concepts of electronic Weyl semimetals [14–17] have been extended to magnon bands in the breathing pyrochlore antiferromagnets [18], as well as collinear ferromagnets [19–22], and other bosonic quasiparticles [23, 24]. In contrast to WMs in collinear ferromagnets [19–22], antiferromagnetic WMs can occur in the absence of DMI. In addition, antiferromagnets have no net spontaneous magnetization. Thus far, the breathing pyrochlore antiferromagnet is the only antiferromagnetic system exhibiting WM nodes [18], but their existence in this system is not very clear as they require broken TRS by the magnetic order and the WM nodes also occur above the lowest magnon band. As every magnetically ordered system breaks TRS, we do not expect all of them to exhibit WM nodes. Moreover, the population effect prohibits WM nodes above the lowest magnon band from contributing to the low temperature transport properties. Therefore the mechanism for WMs to exist in antiferromagnets requires further investigation as corroborated by the authors [18]. In addition, recent study shows that the DMI can induce gapped topological magnon bands in pyrochlore antiferromagnets [25]. Hence, it is valid to say that the WMs in pyrochlore antiferromagnets may not be robust against the DMI [26].

In this Letter, we predict the existence of different

WMs in 3D stacked frustrated kagomé antiferromagnets, which are endowed with an in-plane 120° non-collinear magnetic order due to intrinsic out-of-plane DMI or easy-plane anisotropy or antiferromagnetic intralayer second nearest-neighbour interaction, as realized in real materials [4–8]. As the conventional in-plane 120° magnetic order has zero scalar spin chirality and preserves certain symmetries, we find no WMs despite the broken TRS by the magnetic order. But the 3D magnon bands in this case form nodal-line magnon (NLM) band degeneracy. We argue that the NLMs are due to an “effective TRS” (i.e. time-reversal + spin rotation and/or mirror reflection), which is preserved by the in-plane 120° non-collinear magnetic order. In stark contrast to NLMs in ferromagnets with zero DMI [21, 27], the NLMs in 3D in-plane 120° non-collinear magnetic order require the out-of-plane DMI for stability.

The existence of Weyl nodes do not necessarily require any special symmetry protection. Similar to electronic systems, Weyl nodes appear in pairs of opposite chiralities, and can be separated in momentum space when TRS is broken [15]. In the current study, a slightly canted 120° spin configuration along the out-of-plane stacking direction form noncoplanar chiral spin texture with nonzero scalar spin chirality, which breaks TRS explicitly and macroscopically. In real materials, noncoplanar chiral spin texture can be achieved either by a small in-plane DMI due to lack of mirror symmetry or by an external magnetic field applied normal to the in-plane magnetic order. We consider the latter case as the in-plane DMI can be negligible in frustrated kagomé antiferromagnets. In this case, we show that the NLMs transform into pairs of WM nodes, which form Weyl cones along the (010) surface Brillouin zone. They come in pairs of opposite chirality and also possess chiral magnon surface state (magnon arc) connecting two projected WM nodes on the (010) surface. Most importantly, the WM nodes come from the lowest magnon excitation. Furthermore, we propose a topological phase diagram as a function of the magnetic field and interlayer coupling as the system transits from two to three dimensions. The current results show that WMs should not be allowed in every magnetically

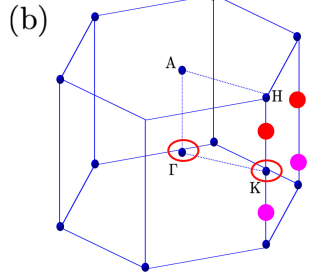
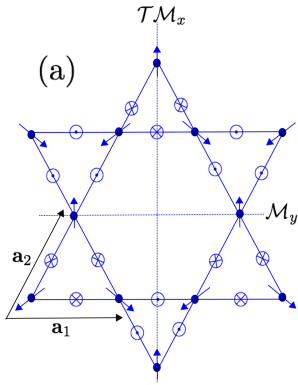


FIG. 1: Color online. (a). Schematics of a single layer kagomé lattice in the 3D unshifted stacking. The 120° non-collinear spin configuration with a positive vector chirality is indicated. The in-plane unit vectors are $\mathbf{a}_1 = (1, 0, 0)$ and $\mathbf{a}_2 = (1/2, \sqrt{3}/2, 0)$. The unit vector along the stacking direction $\mathbf{a}_3 = (0, 0, 1)$ is not depicted. The mirror reflection axes and the direction of DMI are indicated. (b). The first Brillouin zone of 3D hexagonal lattice with indicated high-symmetry points. Open red circles correspond to the locations of NLMs, whereas filled red and pink circles denote WMs on the (010) surface.

ordered antiferromagnets that breaks TRS through the magnetic order. As frustrated kagomé antiferromagnets are 3D in nature, the current prediction of WMs can be experimentally accessible by inelastic neutron scattering.

Model –. We study the 3D stacked kagomé-lattice antiferromagnets governed by the Hamiltonian

$$\begin{aligned} \mathcal{H} = & J \sum_{\langle ij \rangle, \ell} \mathbf{S}_{i, \ell} \cdot \mathbf{S}_{j, \ell} + \sum_{\langle ij \rangle, \ell} \mathbf{D}_{ij} \cdot \mathbf{S}_{i, \ell} \times \mathbf{S}_{j, \ell} \\ & + J_c \sum_{i, \langle \ell \ell' \rangle} \mathbf{S}_{i, \ell} \cdot \mathbf{S}_{i, \ell'} - H \sum_{i, \ell} S_{i, \ell}^z, \end{aligned} \quad (1)$$

where i and j denote the sites on the layers, ℓ and ℓ' label the layers. The first term is the intralayer antiferromagnetic Heisenberg exchange interactions. The second term is a perturbative anisotropy to the Heisenberg exchange interactions, which is dominated by the out-of-plane DMI ($\mathbf{D}_{ij} = \pm D_z \hat{\mathbf{z}}$) due to lack of inversion symmetry between two sites on each layer. The DMI alternates between the triangular plaquettes of the kagomé lattice as shown in Fig. (1). The out-of-plane DMI stabilizes the 120° non-collinear spin configuration and its sign determines the vector chirality of the non-collinear spin order [11, 12]. The third term is the interlayer antiferromagnetic interaction ($J_c > 0$) between the layers. Finally, the last term is an external magnetic field in units of $g\mu_B$; it is along the stacking direction taken as the z -axis. We consider unshifted stacked kagomé layers as realized in different stacked kagomé antiferromagnets [5–8]. Note that in the absence of the magnetic field the out-of-plane DMI breaks the global $\text{SO}(3)$ spin rotation symmetry of the Hamiltonian (1) down to $\text{SO}(2)$ or $\text{U}(1)$ spin rotation symmetry

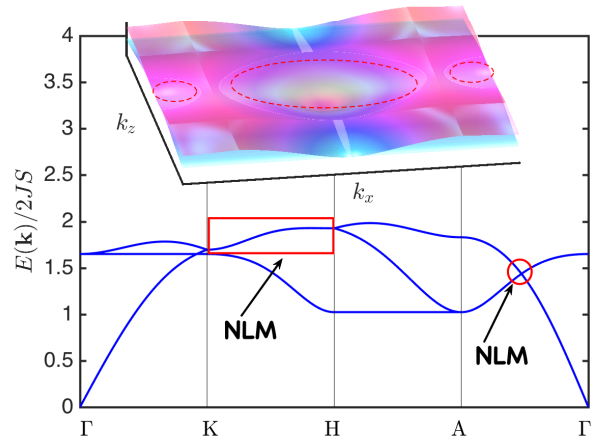


FIG. 2: Color online. Magnon bands of stacked kagomé antiferromagnets at zero magnetic field. Red rectangle and circle indicate the NLMs formed by degenerate bands. Inset shows 3D magnon bands along $k_y = 0$ plane with NLM rings (dashed circles) in the k_x - k_z momentum space. The parameters are $D_z/J = 0.2$, $J_c/J = 0.5$, $H = 0$.

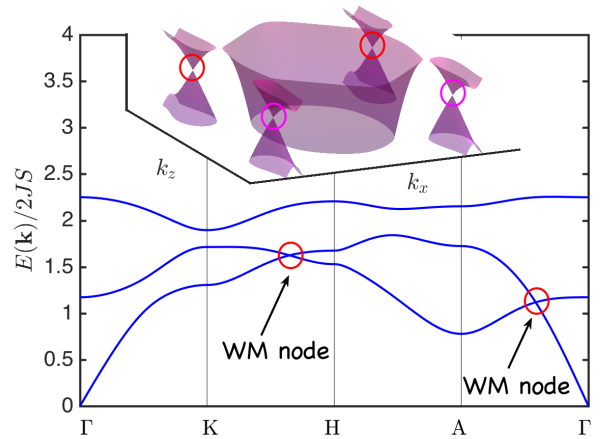


FIG. 3: Color online. Magnon bands of stacked kagomé antiferromagnets at nonzero magnetic field. Inset shows 3D magnon bands along $k_y = 0$ plane for the WM nodes at $(\pm 2\pi/3, 0, \pm k_0^1)$, where red and pink circles indicate opposite chiralities. The parameters are $D_z/J = 0.2$, $J_c/J = 0.5$, $H = 0.3H_s$, where $H_s = 6J + 2\sqrt{3}D_z + 4J_c$ is the saturation field. In this parameter regime there are a total of six Weyl cones in the k_x - k_z momentum space located at $(\pm 2\pi/3, 0, \pm k_0^1)$ and $(0, 0, \pm k_0^2)$.

in the x - y plane or about the z -axis respectively.

Nodal-line magnons –. Now, we study the magnon bands of 3D stacked kagomé-lattice antiferromagnets. In order to do this, we rotate our spin quantization axis locally in spin space so that it aligns with the magnetic ordering; then we introduce the Holstein-Primakoff bosons, see Ref. [28] for detail. In the limit of zero magnetic field ($H = 0$) and zero DMI ($D_z = 0$), the magnon bands of 3D stacked kagomé-lattice antiferromagnets show zero

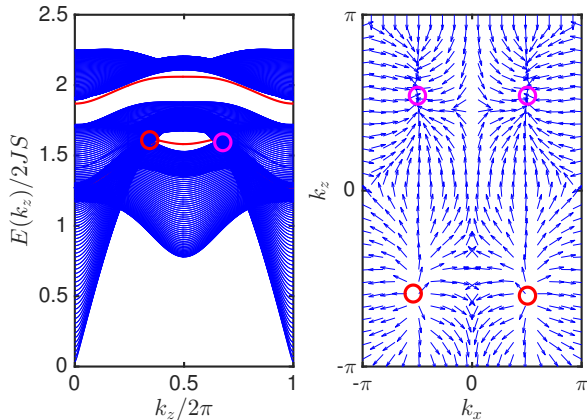


FIG. 4: Color online. (Left). Projected bulk magnon bands (blue region) and WM nodes (red and pink circles) on the $k_y = 0$ plane. Two projected WM nodes (red and pink circles) are connected by a chiral MSS (red lines). (Right). Monopole-antimonopole distribution of the lowest band Berry curvature projected on the $k_y = 0$ plane. Red and pink circles denote WM nodes with chiralities 1 and -1 respectively. The parameters are $D_z/J = 0.2$, $J_c/J = 0.5$, and $H = 0.3H_s$. In this weakly coupled regime the chiral MSS comes from the WM nodes at $(2\pi/3, 0, \pm k_0^1)$ (see Ref. [28] for strongly coupled regime).

modes for specific values of out-of-plane momentum k_z [29, 30]. Therefore the absence of LRO in the 2D kagome antiferromagnets also persists in the 3D limit. As shown in Fig. (2), a nonzero DMI lifts the zero energy mode for all k_z , thereby stabilizes the 3D 120° non-collinear spin configuration as in the 2D system [11]. However, the magnon bands of the 3D system form NLMs (i.e. two magnon bands are degenerate) along K-H and A- Γ lines of the Brillouin zone as depicted in Fig. (2).

The NLMs in the conventional 120° non-collinear spin configurations can be understood as follows. For a perfect kagomé lattice with strong out-of-plane DMI the ground state of the Hamiltonian (1) at zero field is a 120° non-collinear spin configuration with positive vector chirality and zero scalar spin chirality as depicted in Fig. (1). This non-collinear magnetic order preserves all the symmetries of the kagomé lattice. For instance, a combination of TRS (\mathcal{T}) and 180° spin rotation of the in-plane coplanar order about the z -axis, $\mathcal{R}_z(\theta)$, is a good symmetry. In addition, mirror reflection symmetry of the kagomé plane about the x or y axis in combination with \mathcal{T} (i.e. $\mathcal{T}\mathcal{M}_x\mathcal{T}$ or $\mathcal{M}_y\mathcal{T}$) is also a symmetry of the 120° non-collinear magnetic order. These symmetries are referred to as an “effective TRS” and lead to NLMs on any surface not normal to the z -axis. They differ from the NLMs in ferromagnets [21, 27] by the presence of the DMI.

Weyl magnons – We now study the possibility of WMs in the 3D stacked kagomé-lattice antiferromagnets. As we know in electronic systems, Weyl nodes do not require any symmetry protection. They are formed by non-degenerate bands and appear in pairs of opposite chi-

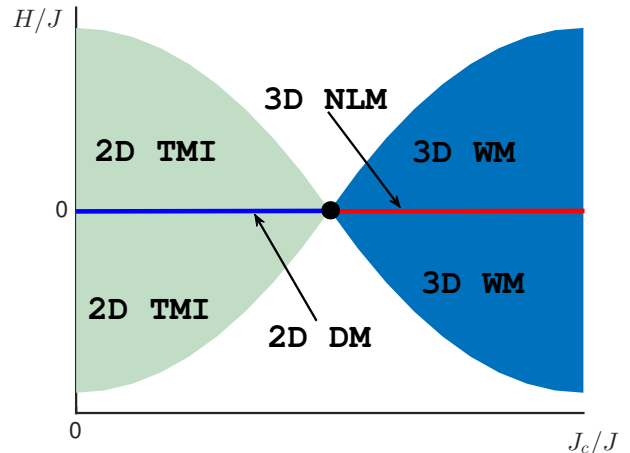


FIG. 5: Color online. Schematic of the proposed topological phase diagram as functions of H/J and J_c/J for $D_z \neq 0$. The blue and red lines correspond to 2D Dirac magnons (DMs) and 3D NLMs respectively at $H/J = 0$. The filled regions correspond to 2D topological magnon insulator (TMI) and 3D WM. The black dot denotes the transition from 2D to 3D system as the interlayer coupling varies. Finally, the uncoloured region is an ordinary insulator phase.

ralities, and can be separated in momentum space when TRS is broken. With this in mind, we expect the 3D in-plane 120° spin configurations to exhibit pairs of WM nodes separated in momentum space when the “effective TRS” is broken. There are two ways in which this symmetry can be broken in this system. First, if the kagomé lattice lacks a mirror plane a small in-plane DMI will be allowed and it can induce noncoplanar chiral spin textures [4]. However, the in-plane DMI is quite negligible in most frustrated kagomé antiferromagnets, e.g. herbertsmithite [13]. Second, applying an out-of-plane external magnetic field normal to the in-plane 120° non-collinear spin configurations can also induce noncoplanar chiral spin textures with nonzero scalar spin chirality given by $\chi = \sum \mathbf{S}_{i,\ell} \cdot (\mathbf{S}_{j,\ell} \times \mathbf{S}_{k,\ell})$ as shown explicitly in Ref. [28].

The interesting thing about magnetic-field-induced scalar spin chirality is that it persists even when the in-plane magnetic order is stabilized by other perturbative interactions different from the DMI, e.g. an easy-plane anisotropy [31] or an intralayer second nearest-neighbour antiferromagnetic interaction [32]. Therefore, WMs can exist in 3D noncoplanar chiral antiferromagnets without the DMI. The magnetic-field-induced noncoplanar chiral spin texture breaks TRS macroscopically, hence we can now look for the existence of WMs. We have confirmed the existence of WM nodes in the noncoplanar regime in Fig. (3). The lowest and middle non-degenerate magnon bands cross linearly in the weakly coupled realistic limit $J_c < J$, and form three pairs of WM cones along the (010) surface located at $(\pm 2\pi/3, 0, \pm k_0^1)$ and $(0, 0, \pm k_0^2)$. In the strongly coupled regime $J_c \geq J$ the topmost and lowest magnon bands cross linearly at $(\pm 2\pi/3, 0, \pm k_0^1)$

and $(0, 0, \pm\tilde{k}_0^2)$ (see Ref. [28]). In both cases, we are able to find the exact analytical form for the locations of the WM nodes (see Ref. [28]). We also find that the WM nodes along K–H line are dominant in the weakly coupled regime $J_c < J$, whereas those along A– Γ line are dominant in the strongly coupled regime $J_c \geq J$. In the main text, we will concentrate on the dominant WM nodes along K–H line for weakly coupled regime $J_c < J$. The analysis for the strongly coupled regime $J_c \geq J$ can be found in Ref. [28]. There are no WM nodes observed for ferromagnetic interlayer coupling ($J_c < 0$) (see Ref. [28]).

It is crucial to point out that the WM nodes in 3D stacked kagomé antiferromagnets differ from those of breathing pyrochlore antiferromagnets [18]. The latter requires no DMI and rely on broken TRS by the magnetic order. However, every magnetically ordered system breaks TRS, but not every ordered magnetic system has WM nodes. Moreover, gapped topological magnon bands were recently found in pyrochlore antiferromagnets with DMI [25]. This suggests that WMs in breathing pyrochlore antiferromagnets may not be robust when all the proper DMIs are taken into account [26]. In the current study, however, the only requirement for the existence of WM nodes is the macroscopically broken TRS by the scalar spin chirality of noncoplanar chiral spin textures, which can be provided by the in-plane DMI or an external magnetic field in addition to the out-of-plane DMI. They also persist even in the absence of DMI as 120° non-collinear magnetic order can be stabilized through other means. As we mentioned above, our results show that WMs should not be allowed in every 3D magnetically ordered system that breaks TRS. An explicit macroscopically broken TRS is indeed required in order to get a direct analog of Weyl fermion semimetals.

Magnon surface states –. The topological protection of WMs is also encoded in the magnon surface states (MSS), which can be regarded as the magnon edge modes on the $k_y = 0$ plane. To see this, we consider a slab with open boundary conditions along x direction and infinite along z direction on the (010) surface. The result is shown in Fig. (4) (left). It shows two projected WM nodes with opposite chirality (red and pink circles) along the k_z direction connected by a chiral MSS (red line). However, two projected WM nodes along the k_x direction have the same chirality, therefore they cannot be connected by a chiral MSS (see Ref. [28]). Also plotted in Fig. (4) (right) is the projection of the Berry curvature for the lowest magnon band on the $k_y = 0$ plane. It shows that the WM nodes act as monopole and anti-monopole of the Berry curvature with chirality 1 (red circle) and -1 (pink circle) respectively. In-between the WM nodes, i.e. $-k_0 < |k_z| < k_0$, the system is gapped and the Chern numbers in the k_x - k_y plane for fixed k_z are estimated as $C_{1,2}(-k_0 < |k_z| < k_0) = \pm\text{sgn}(\sin(\phi))$ for the first two bands and $C_3(-k_0 < |k_z| < k_0) = 0$ for the topmost band, where ϕ is the angle subtended by three noncoplanar spins in a unit triangle (see Ref. [28]), and $\sin\phi$ is proportional to the field-induced scalar spin chirality χ .

Topological phase diagram –. At this juncture, we would like to construct a topological phase diagram. Provided that the in-plane 120° magnetic order is stabilized by the intrinsic out-of-plane DMI ($D_z \neq 0$) or otherwise, a topological phase diagram can be constructed as functions of H/J and J_c/J . In Fig. (5) we propose such topological phase diagram with five distinct phases as H/J and J_c/J are varied. At zero magnetic field ($H/J = 0$ line) and assuming negligible in-plane DMI, there are only two distinct phases — Dirac magnon (DM) nodes in the 2D limit for very small negligible J_c/J , and the NLMs in the 3D limit for non-negligible J_c/J . A nonzero magnetic field induces noncoplanar chiral spin textures, therefore the DM nodes in the 2D limit transform into a 2D topological magnon insulator (TMI) [33]. Whereas the 3D NLMs transform into WMs. The uncoloured white regions correspond to a trivial magnon insulator.

Conclusion –. In summary, the main finding in this Letter is that 3D noncoplanar chiral spin textures in frustrated kagomé magnets can host non-degenerate magnon band touching points in the 3D momentum space. They had been dubbed Weyl magnons (WMs) in analogy to Weyl fermion semimetals. In the current study, the WMs do not rely on the broken TRS by the magnetic order, instead they are provided by the explicit macroscopically broken TRS by the scalar spin chirality of noncoplanar spin textures, giving rise to a direct analog of Weyl fermion semimetals. In real materials with negligible in-plane Dzyaloshinskii-Moriya interaction (DMI) the noncoplanar chiral spin textures can be provided by an external magnetic field applied normal to the in-plane magnetic order.

As physical realistic frustrated kagomé materials are 3D in nature, we believe that our prediction of WMs in noncoplanar chiral spin textures will inspire an experimental search for WMs in frustrated magnets using the inelastic neutron scattering. As we mentioned previously, WMs do not necessarily require the DMI in antiferromagnets as the in-plane 120° magnetic order can also be stabilized by an easy-plane anisotropy or antiferromagnetic intralayer second nearest-neighbour interaction. In this scenario, an external magnetic field still induces noncoplanar chiral spin textures. Similar to gapped 2D topological magnon insulator [33], the current WM nodes in the current study will definitely possess 3D topological thermal Hall effect due to the magnetic-field-induced scalar spin chirality. In fact, as the WM nodes occur at the lowest excitation they will be the dominant contribution to the 3D topological thermal Hall effect. The details of this study will be reported elsewhere [34].

In the current study, we have considered non-collinear spin configurations with positive vector chirality, however our results should also exist in magnetic systems with negative vector chirality as recently reported in a stacked kagomé antiferromagnet [35]. We note that non-collinear spin configurations with negative vector chirality have been reported in metallic frustrated magnets $\text{Mn}_3\text{Sn}/\text{Ge}$

with stacked kagomé-type lattice structure [36–38], and they have been shown to exhibit metallic Weyl points [39, 40]. One of the interesting generalizations of the current study is that Weyl points could be present in chiral spin liquids states [41, 42], where time-reversal symmetry is also broken macroscopically and spontaneously by the scalar spin chirality.

Acknowledgments–. Research at Perimeter Institute is supported by the Government of Canada through Industry Canada and by the Province of Ontario through the Ministry of Research and Innovation.

Note added–. Upon arXiv submission of this manuscript, we became aware of a recent study Ref. [43],

where the authors adopted the easy-plane breathing pyrochlore antiferromagnetic model in Ref. [18], and studied Weyl magnons in the easy-axis counterpart with all-in-all-out (AIAO) magnetic ordering. As we mentioned in the main text, the current results in 3D stacked kagomé antiferromagnets are obviously different from those of (breathing) pyrochlore antiferromagnets. The current results have established that Weyl magnons should not be allowed in every ordered antiferromagnets with broken TRS by magnetic order. An explicit macroscopically broken TRS is indeed required in order to get a direct analog of Weyl fermion semimetals.

-
- [1] M. R. Norman, *Rev. Mod. Phys.* **88**, 041002 (2016).
 - [2] Y. Zhou, K. Kanoda, and T. -K. Ng, *Rev. Mod. Phys.* **89**, 025003 (2017).
 - [3] L. Savary and L. Balents, *Rep. Prog. Phys.* **80**, 016502 (2017).
 - [4] D. Grohol et al., *Nature Materials* **4**, 323 (2005).
 - [5] X. G. Zheng et al., *Phys. Rev. B* **71**, 174404 (2005).
 - [6] X. G. Zheng et al., *Phys. Rev. Lett.* **95**, 057201 (2005).
 - [7] T.-H. Han, J. Singleton, and J. A. Schlueter, *Phys. Rev. Lett.* **113**, 227203 (2014).
 - [8] T.-H Han et al., *Phys. Rev. B* **93**, 214416 (2016).
 - [9] I. Dzyaloshinsky, *J. Phys. Chem. Solids* **4**, 241 (1958).
 - [10] T. Moriya, *Phys. Rev.* **120**, 91 (1960).
 - [11] M. Elhajjal, B. Canals, and C. Lacroix, *Phys. Rev. B* **66**, 014422 (2002).
 - [12] O. Cépas et al., *Phys. Rev. B* **78**, 140405(R) (2008).
 - [13] A. Zorko et al., *Phys. Rev. Lett.* **101**, 026405 (2008).
 - [14] X. Wan, A. M. Turner, A. Vishwanath, and S. Y. Savrasov *Phys. Rev. B* **83**, 205101 (2011)
 - [15] A. A. Burkov and L. Balents, *Phys. Rev. Lett.* **107**, 127205 (2011).
 - [16] S.-Y. Xu et al., *Science* **349**, 613 (2015).
 - [17] B.-Q. Lv et al., *Phys. Rev. X* **5**, 031013 (2015).
 - [18] F.-Y. Li et al., *Nat. Commun.* **7**, 12691 (2016).
 - [19] A. Mook, J. Henk, and I. Mertig, *Phys. Rev. Lett.* **117**, 157204 (2016).
 - [20] S. Ying, X. S. Wang, and X. R. Wang, *Phys. Rev. B* **95**, 224403 (2017).
 - [21] K. Li and J. Hu, *Chin. Phys. Lett.* **34**, 077501 (2017).
 - [22] Ying Su, X. R. Wang, arXiv:1705.04164 (2017).
 - [23] L. Lu et al., *Science* **349**, 622 (2015).
 - [24] V. Peano et al., *Phys. Rev. X* **5**, 031011 (2015).
 - [25] P. Laurell, G. A. Fiete, *Phys. Rev. Lett.* **118**, 177201 (2017).
 - [26] The robustness of Weyl magnons against the DMIs in pyrochlore antiferromagnets is currently not investigated.
 - [27] A. Mook, J. Henk, and I. Mertig, *Phys. Rev. B* **95**, 014418 (2017).
 - [28] See supplemental material for details of spin wave theory of 3D noncoplanar chiral spin texture on the kagomé lattice.
 - [29] D. Schmalfuss, J. Richter, D. Ihle, *Phys. Rev. B* **70**, 184412 (2004).
 - [30] O. Götze and J. Richter, *EPL (Europhys. Lett.)* **114**, 67004 (2016).
 - [31] A. L. Chernyshev, M. E. Zhitomirsky, *Phys. Rev. Lett.* **113**, 237202 (2014).
 - [32] A. B. Harris, C. Kallin, and A. J. Berlinsky, *Phys. Rev. B* **45**, 2899 (1992).
 - [33] S. A. Owerre, *Phys. Rev. B* **95**, 014422 (2017).
 - [34] S. A. Owerre, unpublished.
 - [35] R. Okuma et al., *Phys. Rev. B* **95**, 094427 (2017).
 - [36] H. Chen, Q. Niu, and A. H. MacDonald, *Phys. Rev. Lett.* **112**, 017205 (2014).
 - [37] S. Nakatsuji, N. Kiyohara, and T. Higo, *Nature* **527**, 212 (2015).
 - [38] A. K. Nayak et al., *Sci. Adv.* **2** e1501870 (2016).
 - [39] H. Yang et al., *New J. Phys.* **19** 015008 (2017).
 - [40] J. Kübler and C. Felser, *EPL (Europhys. Lett.)* **108**, 67001 (2014).
 - [41] M. Hermanns, K. O’Brien, and S. Trebst, *Phys. Rev. Lett.* **114**, 157202 (2015).
 - [42] K. O’Brien, M. Hermanns, and S. Trebst, *Phys. Rev. B* **93**, 085101 (2016); Erratum *Phys. Rev. B* **94**, 079908 (2016).
 - [43] S.-K. Jian, W. Nie, arXiv:1708.02948 (2017).

Weyl magnons in noncoplanar stacked kagomé antiferromagnets

Supplemental Material

S. A. Owerre¹

¹*Perimeter Institute for Theoretical Physics, 31 Caroline St. N., Waterloo, Ontario N2L 2Y5, Canada.*

(Dated: September 1, 2022)

A. Spin transformation

In the noncoplanar chiral spin configuration we perform a local rotation about the z -axis by the spin orientated angles θ_i , and then about y -axis by the field-induced canting angle ϑ . The total rotation matrix is given by

$$\mathcal{R}_z(\theta_{i,\ell}) \cdot \mathcal{R}_y(\vartheta) = \begin{pmatrix} \cos \theta_{i,\ell} \cos \vartheta & -\sin \theta_{i,\ell} \cos \theta_{i,\ell} \sin \vartheta & \cos \theta_{i,\ell} \sin \vartheta \\ \sin \theta_{i,\ell} \cos \vartheta & \cos \theta_{i,\ell} \sin \theta_{i,\ell} \sin \vartheta & \sin \theta_{i,\ell} \sin \vartheta \\ -\sin \vartheta & 0 & \cos \vartheta \end{pmatrix}, \quad (1)$$

Now, the spins transform as $\mathbf{S}_i = \mathcal{R}_z(\theta_{i,\ell}) \cdot \mathcal{R}_y(\vartheta) \cdot \mathbf{S}'_i$, where prime denotes the rotated frame. The classical ground state energy is given by

$$E_{\text{cl}} = 3NS^2 \left[2J \left(-\frac{1}{2} + \frac{3}{2} \cos^2 \vartheta \right) - \sqrt{3}D_z \sin^2 \vartheta - J_c(1 - 2 \cos^2 \vartheta) - H \cos \vartheta \right], \quad (2)$$

where N is the number of sites per unit cell, and the magnetic field is rescaled in unit of S . Minimizing this energy yields the canting angle $\cos \vartheta = H/H_s$, where $H_s = 6J + 2\sqrt{3}D_z + 4J_c$ is the saturation field. The free magnon term is given by

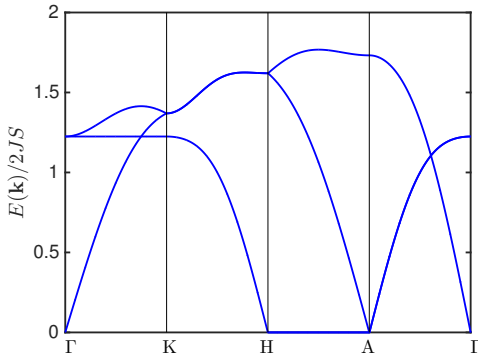


FIG. 1: Color online. Magnon bands for nonzero magnetic field and zero DMI. There is a zero energy mode along H-A line. The parameters for this figure are $D_z/J = 0.0$, $J_c/J = 0.5$, $H = 0$.

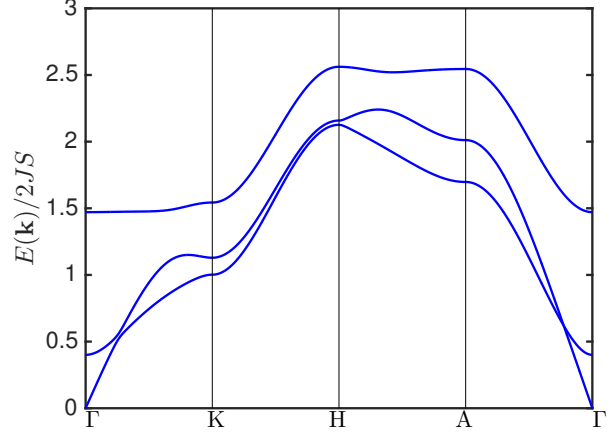


FIG. 2: Color online. Magnon bands with ferromagnetic interlayer coupling. There are no WM nodes. The parameters are $D_z/J = 0.2$, $J_c/J = 0.5$, $H = 0.3H_s$, with $H_s = 6J + 2\sqrt{3}D$.

$$\begin{aligned} \mathcal{H}_J = J \sum_{\langle ij \rangle, \ell} & \left[\cos \theta_{ij,\ell} \mathbf{S}'_{i,\ell} \cdot \mathbf{S}'_{j,\ell} + \sin \theta_{ij,\ell} \cos \vartheta \hat{\mathbf{z}} \cdot (\mathbf{S}'_{i,\ell} \times \mathbf{S}'_{j,\ell}) \right. \\ & \left. + 2 \sin^2 \left(\frac{\theta_{ij,\ell}}{2} \right) (\sin^2 \vartheta S'^x_{i,\ell} S'^x_{j,\ell} + \cos^2 \vartheta S'^z_{i,\ell} S'^z_{j,\ell}) \right], \end{aligned} \quad (3)$$

$$\begin{aligned} \mathcal{H}_{D_z} = -D_z \sum_{\langle ij \rangle, \ell} & \left[\cos \theta_{ij,\ell} \cos \vartheta \hat{\mathbf{z}} \cdot (\mathbf{S}'_{i,\ell} \times \mathbf{S}'_{j,\ell}) \right. \\ & \left. - \sin \theta_{ij,\ell} (\cos^2 \vartheta S'^x_{i,\ell} S'^x_{j,\ell} + S'^y_{i,\ell} S'^y_{j,\ell} + \sin^2 \vartheta S'^z_{i,\ell} S'^z_{j,\ell}) \right], \end{aligned} \quad (4)$$

$$\begin{aligned} \mathcal{H}_{J_c} = J_c \sum_{i, \langle \ell \ell' \rangle} & \left[\cos \theta_{\ell \ell'} \mathbf{S}'_{i,\ell} \cdot \mathbf{S}'_{i,\ell'} \right. \\ & \left. + 2 \sin^2 \left(\frac{\theta_{\ell \ell'}}{2} \right) (\sin^2 \vartheta S'^x_{i,\ell} S'^x_{i,\ell'} + \cos^2 \vartheta S'^z_{i,\ell} S'^z_{i,\ell'}) \right], \end{aligned} \quad (5)$$

$$\mathcal{H}_Z = -H \cos \vartheta \sum_{i,\ell} S'^z_{i,\ell}, \quad (6)$$

where $\theta_{\alpha\beta} = \theta_\alpha - \theta_\beta$. For antiferromagnetic interlayer coupling $J_c > 0$ we have that $\theta_{\ell\ell'} = \pi$. For ferromagnetic interlayer $J_c < 0$ and $\theta_{\ell\ell'} = 0$, therefore only the first term in the J_c term is nonzero. The scalar spin chirality of the non-coplanar (umbrella) spin configura-

tions defined as $\chi = \sum \mathbf{S}'_{i,\ell} \cdot (\mathbf{S}'_{j,\ell} \times \mathbf{S}'_{k,\ell})$ is induced only within the kagomé planes.

B. Holstein-Primakoff transformation

Next, we introduce the Holstein-Primakoff bosons: $S_{i,\ell}^z = S - a_{i,\ell}^\dagger a_{i,\ell}$, $S_{i,\ell}^+ \approx \sqrt{2S} a_{i,\ell} = (S_{i,\ell}^-)^\dagger$, where $S_{i,\ell}^\pm = S_{i,\ell}^x \pm iS_{i,\ell}^y$ and $a_{i,\ell}^\dagger (a_{i,\ell})$ are the bosonic creation (annihilation) operators. In the following we consider the case $J_c > 0$. The case $J_c < 0$ can be derived in a similar way. The magnon hopping Hamiltonians are given by

$$\begin{aligned} \mathcal{H}_{J-D_z} = S \sum_{\langle ij \rangle, \ell} [t^z (a_{i,\ell}^\dagger a_{i,\ell} + a_{j,\ell}^\dagger a_{j,\ell}) \\ + t^r (e^{-i\phi_{ij,\ell}} a_{i,\ell}^\dagger a_{j,\ell} + h.c.) + t^o (a_{i,\ell}^\dagger a_{j,\ell}^\dagger + h.c.)] \end{aligned} \quad (7)$$

$$\begin{aligned} \mathcal{H}_{J_c} = S \sum_{i,\ell} t_c^z a_{i,\ell}^\dagger a_{i,\ell} \\ + S \sum_{i,\langle \ell \ell' \rangle} [t_c^r (a_{i,\ell}^\dagger a_{i,\ell'} + h.c.) + t_c^o (a_{i,\ell}^\dagger a_{i,\ell'}^\dagger + h.c.)], \end{aligned} \quad (8)$$

$$\mathcal{H}_Z = H \cos \vartheta \sum_{i,\ell} a_{i,\ell}^\dagger a_{i,\ell} \quad (9)$$

The solid angle subtended by three non-coplanar spins is given by $\phi_{ij} = \pm\phi$, where $\phi = \tan^{-1}[t_2^r/t_1^r]$. The parameters of the tight binding model are given by

$$t^z = -\left[J \left(-\frac{1}{2} + \frac{3}{2} \cos^2 \vartheta \right) - \frac{\sqrt{3}}{2} D_z \sin^2 \vartheta \right], \quad (10)$$

$$t^r = \sqrt{(t_1^r)^2 + (t_2^r)^2}, \quad (11)$$

$$t_1^r = J \left[-\frac{1}{2} + \frac{3}{4} \sin^2 \vartheta \right] - \frac{\sqrt{3} D_z}{2} \left(1 - \frac{\sin^2 \vartheta}{2} \right), \quad (12)$$

$$t_2^r = -\frac{\cos \vartheta}{2} (\sqrt{3} J - D_z), \quad (13)$$

$$t^o = \frac{\sin^2 \vartheta}{4} (3J + \sqrt{3} D_z), \quad (14)$$

$$t_c^z = 2J_c [1 - 2 \cos^2 \vartheta], \quad (15)$$

$$t_c^r = -J_c [1 - \sin^2 \vartheta], \quad (16)$$

$$t_c^o = J_c \sin^2 \vartheta. \quad (17)$$

Next, we Fourier transform into momentum space using the basis vector $\psi_{\mathbf{k}}^\dagger = (a_{\mathbf{k}1}^\dagger, a_{\mathbf{k}2}^\dagger, a_{\mathbf{k}3}^\dagger, a_{-\mathbf{k}1}, a_{-\mathbf{k}2}, a_{-\mathbf{k}3})$. The resulting Hamiltonian is given by

$$\mathcal{H}(k_{\parallel}, k_z) = 2S \begin{pmatrix} \mathcal{G}^0(k_z) + \mathcal{G}^r(k_{\parallel}) & \mathcal{G}^o(k_{\parallel}, k_z) \\ \mathcal{G}^o(k_{\parallel}, k_z) & \mathcal{G}^0(k_z) + \mathcal{G}^r(k_{\parallel}) \end{pmatrix}. \quad (18)$$

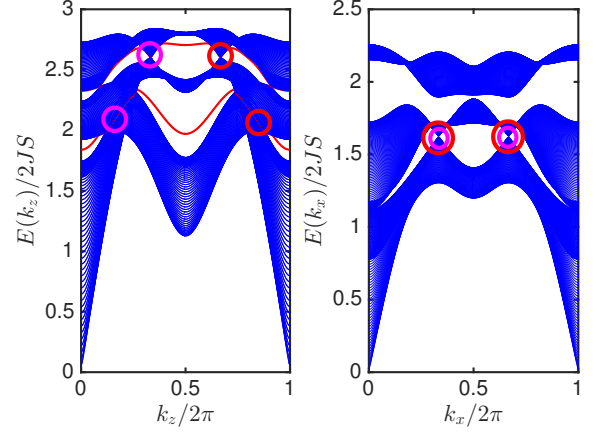


FIG. 3: Color online. Projected bulk magnon bands (blue region) and WM nodes (red and pink circles) on the $k_y = 0$ plane. (Left). Two projected WM nodes (red and pink circles) along the k_z -axis are connected by a chiral MSS (red lines) as they have opposite chirality. Here we set $D_z/J = 0.2$, $J_c/J = 1.2$, $H = 0.3H_s$. In this strongly coupled regime the chiral MSS comes from the WM nodes at $(0, 0, \pm k_0^z)$ and $(0, 0, \pm \tilde{k}_0^z)$. (Right). Two projected WM nodes (red and pink circles) along the k_x -axis are not connected by a chiral MSS as they have the same chirality. Here we set $D_z/J = 0.2$, $J_c/J = 0.5$, $H = 0.3H_s$ (see also main text).

where $\mathbf{k} = (k_{\parallel}, k_z)$ and $k_{\parallel} = (k_x, k_y)$. The \mathcal{G} matrices are given by $\mathcal{G}^0(k_z) = [\sqrt{3}D_z + J + J_c + t_c^r \cos k_z] \mathbf{I}_{3 \times 3}$

$$\mathcal{G}^r(k_{\parallel}) = t^r \begin{pmatrix} 0 & \cos k_{\parallel}^1 e^{-i\phi} & \cos k_{\parallel}^3 e^{i\phi} \\ \cos k_{\parallel}^1 e^{i\phi} & 0 & \cos k_{\parallel}^2 e^{-i\phi} \\ \cos k_{\parallel}^3 e^{-i\phi} & \cos k_{\parallel}^2 e^{i\phi} & 0 \end{pmatrix}, \quad (19)$$

$$\mathcal{G}^o(k_{\parallel}, k_z) = \begin{pmatrix} t_c^o \cos k_z & t^o \cos k_{\parallel}^1 & t^o \cos k_{\parallel}^3 \\ t^o \cos k_{\parallel}^1 & t_c^o \cos k_z & t^o \cos k_{\parallel}^2 \\ t^o \cos k_{\parallel}^3 & t^o \cos k_{\parallel}^2 & t_c^o \cos k_z \end{pmatrix}, \quad (20)$$

where $k_{\parallel}^i = k_{\parallel} \cdot \mathbf{a}_i$, with $\mathbf{a}_1 = \hat{x}$, $\hat{\mathbf{a}}_2 = \hat{x}/2 + \sqrt{3}\hat{y}/2$, and $\hat{\mathbf{a}}_3 = -\hat{x}/2 + \sqrt{3}\hat{y}/2$. The momentum space Hamiltonian of $J_c < 0$ can be derived in a similar way. The magnon bands are obtained by numerically diagonalizing $\mathcal{H}(k_{\parallel}, k_z)$ using the generalized Bogoliubov transformation. In the limit of zero magnetic field ($H = 0$) and zero DMI ($D_z = 0$), the magnon bands of 3D stacking of kagomé-lattice antiferromagnets show zero modes for specific values of k_z , see Fig. (1) along H–A line. Therefore the absence of long-range order in the 2D kagome antiferromagnetic systems persist in the 3D limit. As shown in the main text, a nonzero DMI lifts the zero energy mode for all k_z , thereby stabilizes the 120° non-collinear spin configuration as in the 2D system. The magnon bands for ferromagnetic interlayer coupling has no Weyl magnon (WM) nodes as depicted in Fig. (2).

C. Weyl magnon bands

Weyl magnon nodes exist for antiferromagnetic inter-layer coupling. In fact, at $\Gamma_1 = (k_x, k_y) = (\pm 2\pi/3, 0)$ and $\Gamma_2 = (k_x, k_y) = (0, 0)$ the eigenvalues of the Hamiltonian can be found exactly as a function k_z .

At Γ_1 the energy bands are given by

$$[E_0(k_z)]^2 = \frac{1}{2} \left[2(\mathcal{G}^0(k_z))^2 + (t^r)^2 - (t_c^o)^2 - 2(t^o)^2 + 4t_c^o t^o \cos(k_z) - (t_c^o)^2 \cos(2k_z) - 4t^r \mathcal{G}^0(k_z) \cos(\phi) + (t^r)^2 \cos(2\phi) \right] \quad (21)$$

$$[E_{\pm}(k_z)]^2 = \frac{1}{2} \left[(2\mathcal{G}^0(k_z))^2 + 2(t^r)^2 - 2(t_c^o)^2 - (t^o)^2 - 2t_c^o \{2t^o \cos(k_z) + t_c^o \cos(2k_z)\} + 4t^r \mathcal{G}^0(k_z) \cos(\phi) - (t^r)^2 \cos(2\phi) \pm 2\sqrt{3}t^r \sin(\phi) \{2\mathcal{G}^0(k_z) + t^r \cos(\phi)\} \right], \quad (22)$$

where subscript 0 denotes lowest band, whereas \pm denotes middle and topmost bands respectively.

At Γ_2 the energy bands are given by

$$[E_0(k_z)]^2 = \frac{1}{2} \left[2(\mathcal{G}^0(k_z))^2 + (2t^r)^2 - (t_c^o)^2 - 2(2t^o)^2 - t_c^o \{8t^o \cos(k_z) + t_c^r \cos(2k_z)\} + 8t^r \mathcal{G}^0(k_z) \cos(2\phi) + (2t^r)^2 \cos(2\phi) \right] \quad (23)$$

$$[E_{\pm}(k_z)]^2 = \frac{1}{2} \left[(2\mathcal{G}^0(k_z))^2 + (2t^r)^2 - (t_c^o)^2 - 2(t^o)^2 + 4t_c^o t_c^r \cos(k_z) - (t_c^o)^2 \cos(2k_z) - 4t^r \mathcal{G}^0(k_z) \cos(\phi) - 2(t^r)^2 \cos(2\phi) \pm 4\sqrt{3}t^r \sin(\phi) \{\mathcal{G}^0(k_z) - t^r \cos(\phi)\} \right]. \quad (24)$$

The WM nodes correspond to the points where the magnon bands cross linearly with each other along the

k_z momentum direction. The lowest and middle magnon bands cross linearly at $(\pm 2\pi/3, 0, k_0^1)$ and $(0, 0, k_0^2)$, where $k_0^1 = \pm \cos^{-1}(\alpha_1/\beta_1)$ and $k_0^2 = \pm \cos^{-1}(\alpha_2/\beta_2)$,

$$\alpha_1 = 3(t^o)^2 + 12t^r \cos(\phi)(1 + \sqrt{3}D_z) + 12J_c t^r \cos(\phi) - 3(t^r)^2 \cos(2\phi) + 4\sqrt{3}t^r \sin(\phi) + 12D_z t^r \sin(\phi) + 4\sqrt{3}J_c t^r \sin(\phi) + \sqrt{3}(t^r)^2 \sin(2\phi), \quad (25)$$

$$\beta_1 = 4[3t_c^o t^o - 3t^r t_c^r \cos(\phi) - \sqrt{3}t^r t_c^r \sin(\phi)], \quad (26)$$

$$\alpha_2 = -3(t^o)^2 + t^r \left[6(1 + \sqrt{3}D_z + J_c) \cos(\phi) + 3t^r \cos(2\phi) + 2\{3D_z + \sqrt{3}(1 + J_c - t^r \cos(\phi))\} \sin(\phi) \right], \quad (27)$$

$$\beta_2 = 6t_c^o t^o - 2t^r t_c^r \{3 \cos(\phi) + \sqrt{3} \sin(\phi)\}. \quad (28)$$

The topmost and lowest magnon bands cross linearly at $(\pm 2\pi/3, 0, \tilde{k}_0^1)$ and $(0, 0, \tilde{k}_0^2)$, where $\tilde{k}_0^1 = \pm \cos^{-1}(\tilde{\alpha}_1/\tilde{\beta}_1)$, $\tilde{k}_0^2 = \pm \cos^{-1}(\tilde{\alpha}_2/\tilde{\beta}_2)$

$$\tilde{\alpha}_1 = 3(t^o)^2 + 12t^r \cos(\phi)(1 + \sqrt{3}D_z) + 12J_c t^r \cos(\phi) - 3(t^r)^2 \cos(2\phi) - 4\sqrt{3}t^r \sin(\phi) - 12D_z t^r \sin(\phi) - 4\sqrt{3}J_c t^r \sin(\phi) - \sqrt{3}(t^r)^2 \sin(2\phi), \quad (29)$$

$$\tilde{\beta}_1 = 4[3t_c^o t^o - 3t^r t_c^r \cos(\phi) + \sqrt{3}t^r t_c^r \sin(\phi)], \quad (30)$$

$$\tilde{\alpha}_2 = -3(t^o)^2 + t^r \left[6(1 + \sqrt{3}D_z + J_c) \cos(\phi) + 3t^r \cos(2\phi) + 2\{3D_z - \sqrt{3}(1 + J_c - t^r \cos(\phi))\} \sin(\phi) \right], \quad (31)$$

$$\tilde{\beta}_2 = 6t_c^o t^o - 2t^r t_c^r \{3 \cos(\phi) - \sqrt{3} \sin(\phi)\}. \quad (32)$$

In Fig. (3) we have shown projected WM nodes on the $k_y = 0$ plane. It is evident that two projected WM nodes along the k_z direction are connected by a chiral magnon surface state (MSS). In the strongly coupled regime $J_c \geq J$ the chiral MSS comes from the WM nodes at $(0, 0, \tilde{k}_0^1)$ and $(0, 0, \tilde{k}_0^2)$ as they are the dominant ones (left). Whereas in the weakly coupled regime $J_c < J$ the chiral MSS comes from the WM nodes at $(\pm 2\pi/3, 0, k_0^1)$ (see main text). As mentioned in the main text, two projected WM nodes along the k_x -axis on the $k_y = 0$ plane have the same chirality, therefore they cannot be connected by a chiral MSS (right).